

Monopole defects and magnetic Coulomb blockade

This article has been downloaded from IOPscience. Please scroll down to see the full text article.

2011 New J. Phys. 13 023023

(<http://iopscience.iop.org/1367-2630/13/2/023023>)

View [the table of contents for this issue](#), or go to the [journal homepage](#) for more

Download details:

IP Address: 131.251.133.28

The article was downloaded on 11/04/2012 at 09:43

Please note that [terms and conditions apply](#).

Monopole defects and magnetic Coulomb blockade

Sam Ladak¹, Dan Read¹, Tolek Tyliczszak², Will R Branford^{1,3}
and Lesley F Cohen¹

¹ Blackett Laboratory, Imperial College, Prince Consort Road,
London SW7 2AZ, UK

² Advanced Light Source, Lawrence Berkeley National Laboratory,
MS 6-2100 Berkeley, CA 94720, USA

E-mail: W.Branford@imperial.ac.uk

New Journal of Physics **13** (2011) 023023 (10pp)

Received 17 September 2010

Published 10 February 2011

Online at <http://www.njp.org/>

doi:10.1088/1367-2630/13/2/023023

Abstract. Magnetic monopoles, predicted by Dirac, entered a new paradigm with the discovery of emergent monopoles within dipole lattices known as bulk and artificial spin ices. The observation of monopoles in certain artificial systems, and their absence from other similar structures, is a significant puzzle. Connected artificial spin-ice structures attract much attention in terms of the possibility to read states electrically, and offer the possibility of monopole defect control via well-understood domain wall processes. Nevertheless, full comprehension of the underlying processes is lacking. Here, we establish one of the overriding components. We demonstrate using high-resolution scanning transmission x-ray microscopy (STXM) the cooperative process associated with two transverse domain walls that creates the monopole defect in NiFe. The feature size of the array is large compared to the exchange length in the ferromagnet, and the two transverse domain walls give a rich internal structure to the monopole defect vertex. The magnetic Coulomb repulsion between two domain walls carrying the same sign of magnetic charge stabilizes the monopole defects at fields greater than the depinning field for a single wall at that vertex. These observations allow us to form an overview of monopole defect control possibilities from extrinsic pinning as in Co arrays (the extreme extrinsic limit being isolated bar structures) to intrinsic pinning captured here.

 Online supplementary data available from stacks.iop.org/NJP/13/023023/mmedia

³ Author to whom any correspondence should be addressed.

Spin-ice materials have been studied intensively over the last 10 years and have been shown to be model systems to study frustration [1, 2]. These materials have a pyrochlore structure, and magnetic moments (μ) of approximately $10\mu_B$ are located at the corners of the tetrahedra. The minimum energy configuration is when two spins point into a tetrahedron, and two point out of a tetrahedron. This configuration is known as the ice rules, due to similarities to the bonding in water ice. A recent theoretical treatment [3] has proposed an alternative model of spin ice whereby the magnetic moments are considered to be ‘dumbbells’ with magnetic charges of $\pm q$ localized at the centres of the tetrahedra. Using this model the ice rules translate to a configuration where there is a magnetic charge of zero at the centres of the tetrahedra. The model goes on to predict that a spin flip on the lattice leads to an ice-rule-violating defect with finite magnetic charges of $\pm 2q$ on the centres of adjacent tetrahedra. Once formed, these magnetic charges propagate by further spin flips at an energy cost solely associated with the magnetic Coulomb interaction, creating charge-carrying quasiparticle excitations above the ground state with no conserved magnetic moment. These intrinsic quasiparticles act as sources and sinks of \mathbf{H} and \mathbf{M} , and hence may be considered magnetic monopoles [3]. There is now overwhelming evidence that these monopoles indeed exist, carry a magnetic charge of $5\mu_B\text{\AA}^{-1}$ and obey a magnetic Coulomb’s law; see for example [4].

Artificial spin-ice materials [5] made up of arrays of magnetic nanobars of length l , width w and thickness t , arranged in a geometrically frustrated structure, share a great deal, conceptually speaking, with the parallel field of bulk pyrochlores. In the nanoarrays the magnetic charge $q = \mu/l$ holds; however, unlike in the bulk, μ is no longer a fundamental quantity of a magnetic atom, but rather governed by the saturation magnetization M_S of the ferromagnet and the volume of the bars. Thus ideally $q = M_S t w$ and can be continuously tuned by choice of material and bar dimensions. The Sherrington–Kirkpatrick [6] replica mean-field description of spin glasses forms the basis of algorithms for neural network computation. Frustrated atomic moments offered no prospect of creating neural network hardware because the spins could not be individually read, written or manipulated. Intriguingly all of that functionality is already available for artificial spin-ice nanostructures, so neural network reconfigurable logic hardware is a realizable possibility.

For any nanostructured array of identical bars, the sum charge at a vertex, Q , is effectively quantized into integer multiples of q and the magnetic charge carriers have $Q = \pm 2q$. In a square lattice, a zero magnetic charge (two-in, two-out) state can be realized, but on a honeycomb lattice three bars meet at each vertex and the ice rule leaves residual magnetic charge ($Q = \pm q$) at each vertex, a state known as ‘Kagome spin ice’ [7]. The vertex charge influences the charge carriers at short range, creating a Coulombic pinning potential [8] and hence playing a role in the magnetic switching [9, 10]. Note that we reserve the term ‘monopole’ for the highly symmetric $Q = \pm 3q$ ice-rule defect rather than using it as a generic term for a magnetic charge carrier.

In the natural pyrochlores, the monopoles propagate by the flipping of atomic magnetic moments. In the nanostructures, the monopoles are formed by the switching of nanobar moments, which occurs by the nucleation and propagation of domain walls. The latter can be considered to be the magnetic charge carriers in our system. The magnetic field at which magnetic charge flows is determined by the fields at which domain walls are depinned or nucleated. In our permalloy arrays, the edge nucleation fields and internal depinning fields are much lower than internal nucleation fields, so the magnetic charge flows by propagation of domain walls from edge to edge, and the switching transition is complete before the

intra-array nucleation field is reached. In this paper, we make a distinction between intrinsic and extrinsic pinning. We define intrinsic pinning as the pinning that results from on-site carrier-vertex magnetic Coulomb interactions defined by the geometry of the array and the magnetic properties from which the array is formed. The Coulomb interactions are independent of which vertex the charge is traversing, and if only intrinsic pinning were present and the array were perfectly regular and infinite, all bars would switch at the same magnetic field and monopole defects would never be observed in the array [9, 10]. We define extrinsic pinning as pinning due to quenched disorder; in reality the vertices in our arrays are not perfectly identical and the intrinsic pinning potentials are modified by variations in wire width and thickness, and by defects produced by the nanostructuring process. Extrinsic pinning causes different bars to switch at different fields. When extrinsic pinning dominates, monopole defects can be trapped at specific vertices with higher than average domain wall depinning fields, as we previously observed in cobalt honeycombs [8]. In this context, a honeycomb array of isolated bars [11] can be considered as the infinite pinning regime where a domain wall must be nucleated for each switching event.

For both applications and fundamental studies of magnetic charge carriers [9, 12], it is desirable to avoid local, extrinsic pinning of the charge. NiFe is the material of choice for many nanomagnetic applications [13]–[15] where pinning is minimized; thus the formation and internal structure of monopole defects in NiFe structures are of particular interest. Here we describe an intrinsic mechanism of monopole defect formation based on the magnetic Coulomb interactions between two domain walls trying to move onto the same vertex. As each wall prevents the transit of the other, we term this ‘magnetic Coulomb blockade’.

In this paper, we image monopole defects at ultra-high resolution using scanning transmission x-ray microscopy (STXM) and study their formation using OOMMF (Objected Orientated Micro-Magnetic Framework) simulations [16]. Figure 1 sets out a number of possible monopole defect formation scenarios. Previously we have established [8] that magnetic monopole defects are created in cobalt honeycombs after a conditioning routine by the pathway represented in figures 1(a) and (b) by a single bar switching event. The monopole defect is stabilized by large extrinsic domain wall pinning fields.

The strong differences in domain wall depinning fields [17] between magnetically soft NiFe (with virtually no magnetocrystalline anisotropy and magnetostriction allowing the magnetic properties to be dominated by the shape of the wire) and Co (which is magnetically harder) may provide a clue to why monopole defects in connected permalloy honeycombs have remained so elusive [10, 18, 19].

Here we study two permalloy honeycomb samples, which were fabricated by e-beam lithography on SiN membranes, evaporation of Ni₈₁Fe₁₉ and lift-off. One is composed of 8 nm thick permalloy with nanobar dimensions of $w = 100$ nm and $l = 1$ μ m and a spatial extent of $(100 \mu\text{m})^2$. The other is composed of $t = 16$ nm permalloy and has the same nanobar dimensions and a smaller spatial extent $(8 \mu\text{m})^2$. Note that the film thickness is chosen to ensure that transverse domain walls [20] persist in permalloy honeycomb structures [10, 21]. Room temperature STXM studies were carried out on beamline 11.02 at the Advanced Light Source (Berkeley, CA, USA). The sample was mounted in the STXM chamber between the pole pieces of an electromagnet, which allowed the application of an in-plane field of ± 60 mT *in situ*. The chamber was pumped down to a pressure of approximately 100 mT before filling with He gas. Elliptically polarized x-rays were provided by an undulating beamline after which they were focused to a spot size of approximately 30 nm using a Fresnel zone plate. The sample

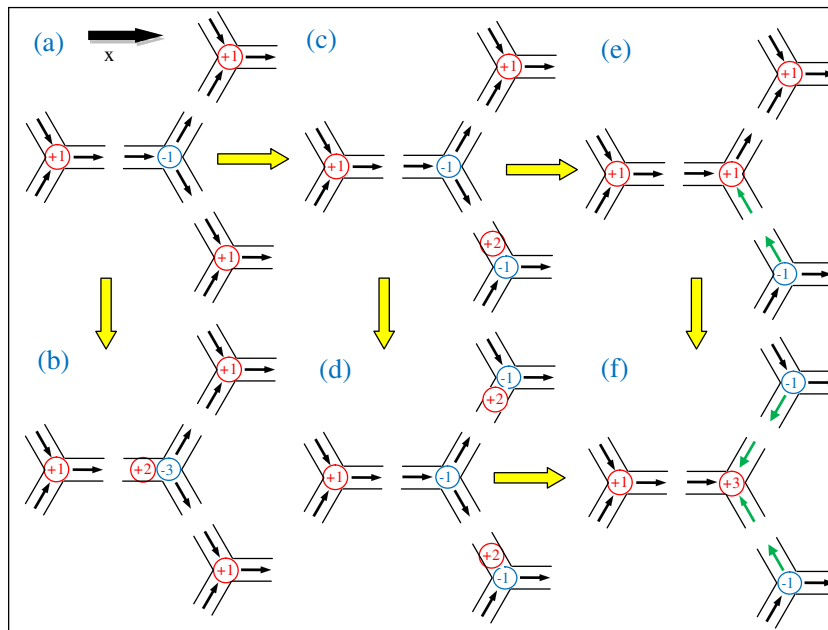


Figure 1. Monopole formation scenarios. The magnetization (black arrows) can be thought of as equal and opposite magnetic charges separated by a single bar length. The sum of these charges are shown by red (net positive charge) and blue circles (net negative charge): (a) initial (saturated) state (with field applied along positive x -direction) that survives to remanence. (b) $\Delta Q = 2$ monopole vertex formed when negative applied field causes a +2 domain wall nucleation at a -1 vertex simultaneously forming a -3 monopole vertex. (c) Field-induced +2 domain wall nucleation at a +1 vertex, (d) double domain wall vertex and (e) ice-rule vertex with magnetic charge disorder and (f) $\Delta Q = 4$ monopole vertex.

and electromagnet were mounted at approximately 30° with respect to the x-ray propagation vector, which allowed the in-plane component of the magnetization to be probed using the x-ray magnetic circular dichroism (XMCD) effect. Micromagnetic simulations were performed with the OOMMF [16]. A cell size of 5 nm was used to construct the mesh, and the magnetization was allowed to relax in the absence of an applied magnetic field in order to find a minimum energy configuration. The magnetocrystalline anisotropy of $\text{Ni}_{81}\text{Fe}_{19}$ was assumed to be zero, the exchange stiffness was taken to be $1.3 \times 10^{-11} \text{ J m}^{-1}$, and the saturation magnetization was assumed to be 800 emu cm^{-3} .

After saturating the magnetization in the positive x -direction, we took large area STXM images in increasing negative field steps until a monopole defect was located in the image, and then collected a high-resolution image at that vertex. In the 16 nm thick array, this occurred at 6.0 mT and is shown in figure 2(a). The two bright areas that can be seen just off the vertex centre suggest that a monopole defect consists of two transverse domain walls. We then returned to zero field and collected a high-resolution image at the same vertex. The monopole defect with magnetic charge $-3q$ (3-out state) persists at remanence, and is shown in figure 2(b). Both the creation of monopole defects at particular fields and their survival at remanence suggest that once formed they are pinned to a site and are important observations.

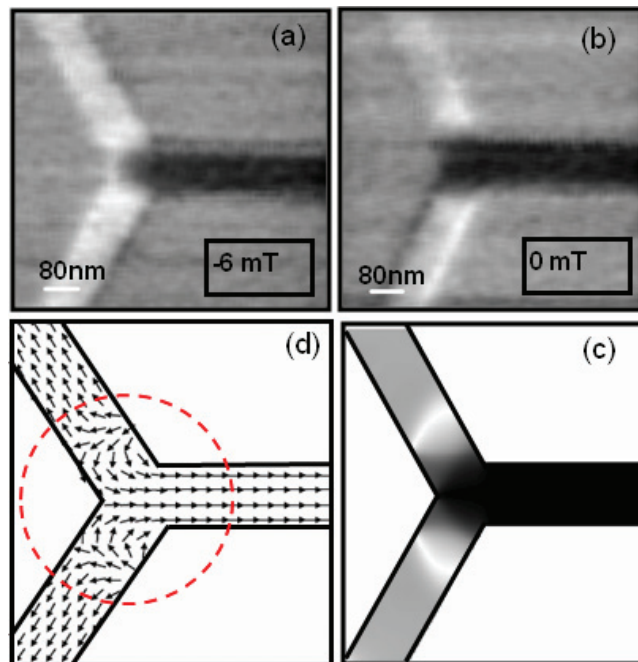


Figure 2. Monopoles at high resolution. Black colour contrast represents magnetization with a positive x -component and white represents magnetization with a negative x -component. (a) A high-resolution STXM image of a monopole defect $-3q$ state in -6.0 mT field. (b) A high-resolution STXM image of a monopole defect $-3q$ state in remanence at zero field, formed by the application of a preconditioning field of -6.0 mT. A micro-magnetic simulation of (c) the contrast map of the x -component of magnetization and (d) the micro-magnetic configuration of a $-3q$ monopole defect state. The dashed circle (radius ~ 150 nm) indicates the extent of distortion from the idealized 3-out state.

The observation of a two-domain wall state was investigated further by micromagnetic simulations [16]. Figure 2(c) shows a $-3q$ monopole defect state produced by the simulations at remanence, in excellent agreement with the experimental image. The simulated nanomagnetic configuration is shown in figure 2(d). The simulations confirm that two transverse domain walls are present and are pinned off the vertex centre. The x -component of the dipole moment (m_x) of the core of the two transverse domain walls is anti-aligned with the moment on the horizontal nanowires. This forces the opposite sign of m_y in the walls and therefore implies opposite chirality with respect to the local Ising axis (magnetization direction). Note that the vertex is large (> 100 nm) compared with the exchange length in permalloy (5 nm) and it is interesting that on lengthscales less than the array feature size (wire width), the monopole defect vertex contains topologically conserved entities (transverse domain walls) with finite dipole moment. Distortions from the idealized picture of a monopole defect on an Ising spin lattice extend up to 150 nm from the vertex centre. The asymmetry here appears much more pronounced than in the monopole defects formed by a single wall extrinsic pinning process in cobalt honeycombs [8].

Returning to the question of the relationship of monopole defects to the reversal process in the array, we can construct an effective M-H loop by taking images in many applied fields.

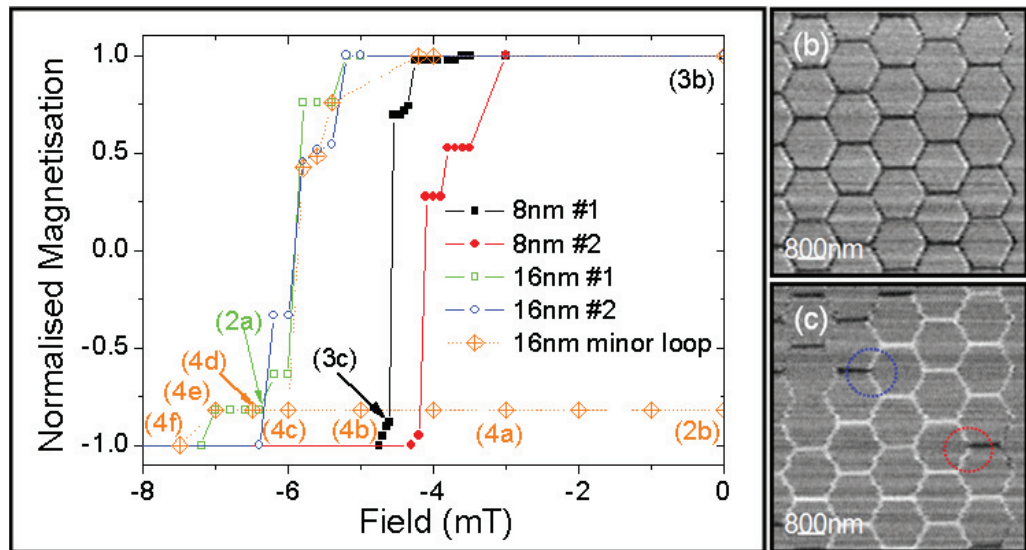


Figure 3. Monopoles in the switching process. (a) A digital hysteresis loop constructed from images for numerous magnetic reversals. Where a data point corresponds to a specific figure, the figure number is indicated in parentheses. The normalized magnetization was obtained by taking the ratio of the number of bars with positive M_x to those with negative M_x for each field value. Five separate reversals are shown: a 8 nm film, sweep 1 (black squares) and sweep 2 (red circles). A 16 nm film, sweep 1 (open green squares) and sweep 2 (blue circles). A 16 nm minor loop (orange crosses). STXM image of a honeycomb structure at (b) 0 mT and (c) -4.65 mT. Black colour contrast indicates that the magnetization has a positive component of magnetization, whereas white indicates a negative x -component.

During several field cycles monopole defects were found at fields between 4 and 5 mT in the 8 nm array and 6 and 7 mT in the 16 nm array, confirming the observations shown in figure 2. Figure 3(a) shows the reverse segment of the M-H loops. Two example large-area STXM images of the 8 nm array at remanence and at -4.65 mT are shown in figures 3(b) and (c) and the full set of images for that switching transition are shown in supplementary figure 1, available at stacks.iop.org/NJP/13/023023/mmedia. At remanence all the bars have positive m_x , whereas at -4.65 mT the majority of bars have switched to having a negative m_x . Two monopole defects are captured in this image, as highlighted by the dotted circles. Interestingly, monopoles are observed only in fields close to the end of the field reversal process, in contrast to Co honeycombs where monopoles formed preferentially at the beginning of the field reversal process [8].

To study the monopole defect depinning process in more detail, high-resolution images were collected at the same vertex in increasing negative field steps on the reverse leg of the minor loop (after preconditioning). These images are shown in figures 4(a)–(f). As the field increases, the two tail–tail domain walls are pushed together on to the vertex, and m_x becomes increasingly negative within the walls. At a field of approximately 7.5 mT (16 nm array), the monopole is depinned as a domain wall propagates along the horizontal bar, switching the vertex into an ice-rule state with all bars having a negative magnetization component. Companion micro-magnetic

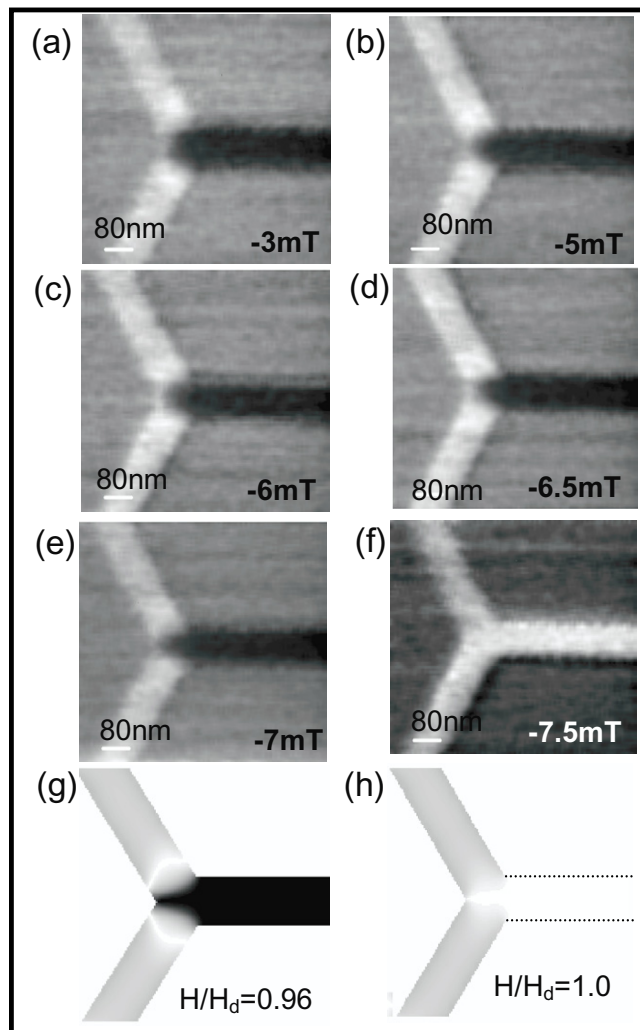


Figure 4. Monopole defects under magnetic pressure. (a–f) STXM images of the $-3q$ monopole defect in figure 2(a) in a magnetic field along the negative x -direction. (g, h) Micromagnetic simulations of a $-3q$ monopole defect in the application of an applied magnetic field close to H_d . Note that the zero-temperature nature of the OOMMF code means that, to make meaningful comparison to the experimental data, the field scale is normalized to the monopole depinning field (H_d).

simulations of a single vertex that had been preset to a $-3q$ state are shown in figures 4(g)–(h) and in supplementary figure 2, available at stacks.iop.org/NJP/13/023023/mmedia. Here the movement of the domain walls towards each other is captured as is the monopole depinning field (H_d).

The underlying magnetic charge distribution in the simulations shown in figures 2(b) and 4(g) is plotted in figures 5(a) (remanence) and 5(b) ($0.96H_d$), respectively. Even at remanence, both domain walls are seen to be distorted, with a complex asymmetric charge distribution [22]. A simplified point-charge model of the coercive field of honeycombs has been proposed [9, 10]. A magnetic point charge Q is driven by an applied field (H) with a

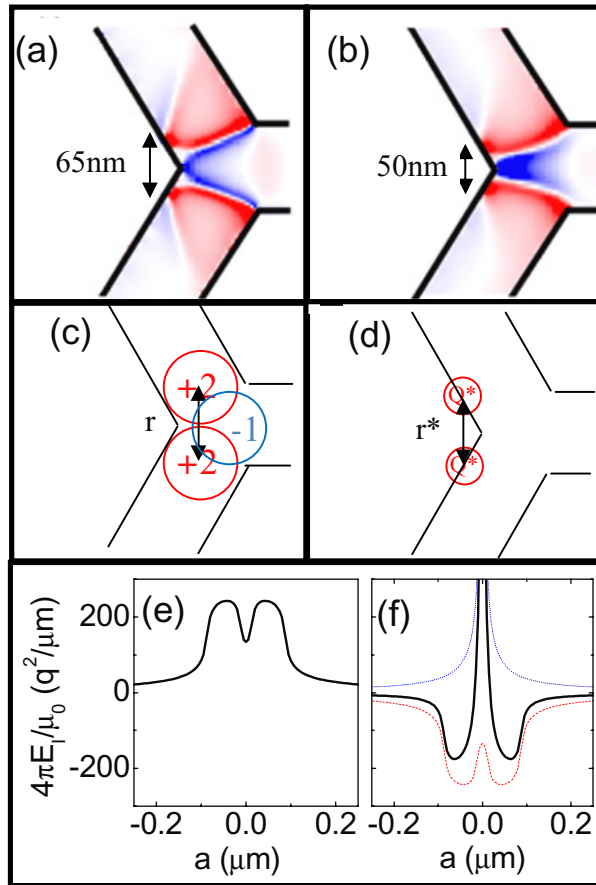


Figure 5. Effective magnetic charge model. (a, b) The magnetic charge density distribution at the monopole defect in the micromagnetic simulations (a) in zero field (figure 2(c)) and (b) in a field close to the monopole depinning field ($H/H_d = 0.96$, figure 4(g)). Red corresponds to negative charge density and blue corresponds to positive charge density. Arrows indicate separation between regions of maximum positive charge density. (c) Simple diagram demonstrating point-charge model, where each domain wall is represented by a point charge of $-2q$. (d) Modified point-charge model, where the unscreened regions of maximum magnetic charge density are used to calculate the depinning field. (e) Energy profile demonstrating the interaction between a domain wall ($+2q$) and the complex magnetic charge distribution at a vertex ($\pm q$). (f) Single domain wall pinning profile (red dotted line), magnetic Coulomb repulsive energy profile (blue dotted line) and the sum of the two energy profiles, which is seen by two domain walls pinned at a vertex (black solid line).

force $F = \mu_0 H Q$. Equating the coercive force for switching the bars (H_C), to the Coulomb force (F_C) for separating a DW with charge $Q = 2q$ from vertex $Q = -q$ at a separation corresponding to the DW size (approximately the wire width w) yields $\mu_0 H_C = F_C / 2q = 2 \mu_0 q^2 / 4(2q)\pi w^2 = \mu_0 M_{St} / 4\pi w$. This corresponds to a coercive field of 12.8 mT for the 16 nm array and 6.4 mT for the 8 nm array. Similarly, one could estimate that the monopole

depinning field to force two DWs with like charge onto the same vertex at separation w is $\mu_0 H_d = F_d/2(2q) = \mu_0(2q)^2/8(2q)\pi w^2 = \mu_0 M_{St}/4\pi w$. This predicts identical depinning and coercive fields. Therefore, the depinning field H_d is equivalent to the coercive field H_C contrary to our observation that the monopoles persist after the other bars have switched ($H_d > H_C$).

We can use the OOMMF simulated magnetic charge maps in figure 5 to refine the point-charge model with effective magnetic charge Q^* and these effective separations, r^* , giving effective Coulomb force $F^* = \mu_0 Q^{*2}/4\pi r^{*2}$. We define the effective charge separation, r^* , as the separation of the two regions of maximum positive magnetic charge density in figures 5(a) and (b), which gives $r_0^* = 65$ nm at remanence (H_0) and $r_d^* = 50$ nm at $H_d \sim 7.5$ mT. Equating the applied compressive force from the field ($F = 2\mu_0 H(2q)$ as there are no near-field issues) to the measured magnetic charge compression, $4\mu_0 q(H_d - H_0) = \mu_0 Q^{*2}/4\pi \cdot [1/r_d^{*2} - 1/r_0^{*2}]$ and rearranging, we obtain effective charge $Q^* = 1.36q$. Note that the finite r_0^* describes the potential well holding the two DWs close to the vertex (figures 5(e)–(f)). Extending the proposal that it is the vertex-wall magnetic charge interaction that controls the coercive field [9, 10], we crudely test the effective charge model. Applying to the $t = 8$ nm array the same values of r_0^* , r_d^* and $Q^*(q = M_{St}w)$ and rearranging for H_d , we obtain $H_d = 4.8$ mT, in good agreement with the measured value of 4.8 mT. Furthermore, if we modify the coercive field calculation to use the effective charge for the local interaction with the vertex, we obtain $\mu_0 H_C = F_C/2q = \mu_0 q Q^*/4(2q)\pi w^2$, which gives coercive fields of 8.32 mT for the 16 nm array and 4.16 mT for the 8 nm array, in excellent agreement with the measured switching fields in figure 3(a). This suggests that the model at least captures the scaling of the coercive field with t/w [23] in the $t \ll w$ regime.

The interaction between a domain wall ($+2q$) and the complex magnetic charge distribution at a vertex ($\pm q$) produces a complex pinning profile [8, 24] (figures 5(e) and (f)). In the double-wall case there is an additional effective magnetic Coulomb force between the walls $F^* = \mu_0 Q^{*2}/4\pi r^{*2}$ (figure 5(f)). This phenomenological model describes well the observed equilibrium wall separation, the persistence after the switching of all other bars, and the survival at remanence of the monopole defects.

There are significant differences between the behaviour of permalloy and Co monopole defects in connected nanostructures. In permalloy, quenched disorder plays a greatly reduced role, the majority of bars switch in long cascades [10] in a single field step, and the observed monopoles began as ice-rule vertices of opposite charge, with $\Delta Q = +4$ in a single preconditioning field step. The monopole creation in permalloy is closer to the scenario shown in figures 1(a)–(f). This work provides insights into the range of monopole defect control limits that can be engineered through material choice and structure. Extreme pinning can be created by structures with isolated bars [11] and moderate pinning can be created by choice of a material with strong magnetic anisotropy such as Co [5]. The intrinsic or weak pinning limit captured here allows for efficient domain wall transfer through connected magnetic nanowire networks, ideal for applications that rely on the creation of monopole currents.

In conclusion, in the weak pinning regime of connected permalloy honeycombs, monopole defect formation is a cooperative process involving two strongly correlated transverse domain walls. It is a magnetic Coulomb blockade between like-charged domain walls that provides the pinning potential near the vertex centre for monopole defects. The stability of such monopole defects is particularly encouraging for data storage purposes. The observation that monopole defect formation in permalloy requires a spreading of the domain walls into the nanobars indicates that bar length may be a useful parameter for controlling the monopole

defect concentration. This is an important development for ice-rule-based devices, such as the Sherrington–Kirkpatrick [6] parallel processors. Further studies are needed in order to determine whether such defects can be injected into an array in a controlled manner.

Acknowledgments

This work was funded by the EPSRC (grant no. EP/G004765/1; to WRB) and the Leverhulme Trust (grant no. F/07058/AW; to LFC). We are grateful for resources provided by the National Academic Grid. The Advanced Light Source is supported by the US DoE under contract no. DE-AC03-76SF00098. We thank L O’Brien for discussions.

References

- [1] Bramwell S T *et al* 2001 *Phys. Rev. Lett.* **87** 047205
- [2] Bramwell S T *et al* 2001 *Science* **294** 1495–501
- [3] Castelnovo C *et al* 2005 *Nature* **451** 42–5
- [4] Bramwell S T *et al* 2009 *Nature* **461** 956–60
- [5] Wang R F *et al* 2006 *Nature* **439** 303–6
- [6] Sherrington D *et al* 1975 *Phys. Rev. Lett.* **35** 1792–6
- [7] Wills A S *et al* 2002 *Phys. Rev. B* **66** 144407
- [8] Ladak S *et al* 2010 *Nat. Phys.* **6** 359–63
- [9] Tchernyshyov O 2010 *Nat. Phys.* **6** 323–4
- [10] Mellado P *et al* 2010 *Phys. Rev. Lett.* **105** 187206
- [11] Mengotti E *et al* 2010 *Nat. Phys.* **7** 68–74
- [12] Sondhi S 2009 *Nature* **461** 888–9
- [13] Allwood D A *et al* 2005 *Science* **309** 1688–92
- [14] Comstock R L 2002 *J. Mater. Sci., Mater. Electron.* **3** 509–23
- [15] Parkin S S P *et al* 2008 *Science* **320** 190–4
- [16] OOMMF (The OOMMF code is available at <http://math.nist.gov/oommf>)
- [17] Xu P, Xia K, Yang H F, Li J J and Gu C Z *Nanotechnology* **18** 295403
- [18] Qi Y *et al* 2008 *Phys. Rev. B* **77** 094418
- [19] Tanaka M *et al* 2005 *J. Appl. Phys.* **97** 10J710
- [20] Nakatani Y *et al* 2005 *J. Magn. Magn. Mater.* **290** 750–3
- [21] Qi Y 2008 Artificial Kagome spin ice *PhD Thesis* University of Maryland (<http://www.lib.umd.edu/drum/bitstream/1903/8359/1/umi-umd-5665.pdf>)
- [22] Zeng H T *et al* 2010 *J. Magn. Magn. Mater.* **322** 2010–4
- [23] Uhlig W C *et al* 2004 *Appl. Phys. Lett.* **84** 759–61
- [24] Petit D *et al* 2009 *Phys. Rev. B* **79** 214405